Melt Redistribution by Pulsed Compaction within UltraLow Velocity Zones

Saswata Hier-Majumder

Department of Geology,
Center for Scientific Computation and Applied Mathematical Modeling,
University of Maryland
College Park, MD, USA
Department of Earth Sciences
Royal Holloway University of London
Egham, Surrey, UK.

Abstract

This article investigates the melt distribution and resultant seismic signature within UltraLow Velocity Zones (ULVZs) forced by pulsed compaction at the mantle-ULVZ interface. Transient flow in the ambient mantle causes periodic compaction in the ULVZ matrix. For a neutrally buoyant melt, an initially uniform melt distribution is modified by the formation of a thin, decompacting, melt-rich layer near the top and a wide, melt-poor, compacting layer near the bottom. Such a structure is reflected in large reductions in S and P wave velocities near the top and smaller reductions near the bottom of the ULVZ. A dense melt pools near the bottom of the ULVZ, leading to larger reductions in seismic wave speed near the bottom. The magnitude of melt segregation in the decompaction layer is controlled by the viscosity of the ULVZ matrix in a nonlinear fashion. At high ULVZ viscosities, the compaction length becomes substantially larger than the dimension of thin

Email address: Saswata.Hier-Majumder@rhul.ac.uk (Saswata Hier-Majumder)

Preprint submitted to Physics of Earth and Planetary Interiors *January 24, 2014*

ULVZs, leading to a reduction in the magnitude of melt segregation in the decompaction layer. In a ULVZ of matrix viscosity 10^{20} Pas containing an average melt volume fraction of 0.05, formation of decompacting, melt-rich layers reduce the S and P wave velocities by 25% and 8%, respectively. Vertical variation in seismic velocity reduction within the ULVZ column is a consequence of melt redistribution by compaction, rather than variation of melt microstructure within the ULVZ.
Keywords: Core-Mantle Boundary; Two-Phase Flow; ULVZ; Compaction; microgeodynamics

---

1. Introduction

A number of thin, dense UltraLow Velocity Zones (ULVZs), characterized by low seismic shear wave speed appear on the mantle side of the Earth's Core-Mantle Boundary (CMB). The ULVZs, which are up to 10% denser than the surrounding mantle, are characterized by differential reductions of S (up to 30%) and P (up to 10%) wave velocities (Rost et al., 2010, 2006; Williams and Garnero, 1996). The elevated density and body wave speed reduction within the ULVZs indicates that the ULVZs are chemically anomalous compared to the surrounding lower mantle. Such chemical anomaly can arise from a neutrally buoyant interstitial melt hosted in an iron-rich solid matrix (Hernlund and Jellinek, 2010; Ohtani and Maeda, 2001; Stixrude and Karki, 2005). A phase equilibria study by Fiquet et al. (2010) suggests that fertile peridotite reaches its solidus at 4180 K and 135 GPa, implying the likely presence of partial melting within the ULVZ.

The chemically anomalous ULVZs are also dynamically coupled to flow in the surrounding mantle. A number of recent studies demonstrate the two-way nature of this coupling. First, the presence of a ULVZ-like, thin, dense, and low-viscosity layer can anchor mantle plumes to the CMB, and contribute to the longevity of plumes (Jellinek and Manga, 2004). Second, mantle motion-induced stirred compaction within the dense ULVZ redistributes nearly neutrally buoyant melt (Hernlund and Jellinek, 2010). Third, near the margin of Large Low Shear Velocity Provinces (LLSVPs), ULVZ-like structures break-up, coalesce, and are mobilized by circulation internal to the LLSVPs (McNamara et al., 2010). Finally, the curvature and topography of the ULVZ-mantle interface results from dynamic interaction between the mantle and the ULVZ, and is modulated by the density and viscosity of the ULVZ material (Bower et al., 2011; Hier-Majumder and Revenaugh, 2010).

Such transient variation in the ambient mantle flow around a partially molten ULVZ will also redistribute melt by compacting the matrix, leading to spatial and temporal variations in effective elastic properties. In a study of anomalous velocities of the core-reflected ScP phase, Rost et al. (2006) observed a downward increase in seismic wave speed within the ULVZ. They suggested that such an increase likely arises from a change in the melt microstructure from tubules near the top to spherical pockets near the bottom of the ULVZ. Such a conclusion would also imply that the thermodynamic forces that control the melt microstructure, must also display a corresponding variation. The source of such a variation, however, is not clear. In addition to internal variations, forced by transient coupling with mantle flow, seismic signature of different ULVZs will vary based on the nature of the surrounding mantle flow. While Hernlund and Jellinek (2010) studied the effect of an imposed, steady-state matrix velocity on redistribution of melt within a ULVZ, the role of transient compaction on melt redistribution and the seismic signature within ULVZs has not yet been studied.

The nature of time-dependence of the ULVZ compaction is difficult to constrain. On the surface, variations in dynamic topography, driven by mantle flow, can be constrained using various geological and geophysical techniques. At the CMB, constraining the time dependence of mantle flow is much less straightforward, as seismic observations only provide the information at the present time. In the absence of observational constraints, one can describe the transient forcing on compaction of the ULVZ as a sum of a number of periodic variations of various frequencies. One can then study the response of the internal structure of the ULVZ to each individual frequency, over a range of frequencies. This is the approach taken in this article. The time period of such periodic variations should capture relatively rapid gravitational drainage of dense melts and slower oscillatory mass transport through plume conduit waves. In a compacting ULVZ matrix, gravitational drainage can segregate melt, denser than the matrix by a few percents, into a thin layer near the bottom over a few ka (Hier-Majumder et al., 2006). Numerical and analog material experiments indicate that mass is transferred in the plume conduit in periodic, conduit waves with time periods of a few Mas (Olson and Christensen, 1986; Schubert et al., 1989). The time periods intermediate to these two time scales are crucial to understand the structural evolution of the ULVZs in response to the relevant forces. Accordingly, the time periods of pulsation in this study were chosen to provide a glimpse into the response of the ULVZ to both short and long term variations.

As compaction of the matrix redistributes the melt, the elastic properties are also modified. Using robust models of effective elastic properties, one can predict such spatial and temporal variations in the seismic signature. In a recent microgeodynamic model, Wimert and Hier-Majumder (2012) demonstrated that the seismic signature of the ULVZs can be explained by only 0.1 volume fraction of melt residing in tubules. In that study, only average wave speed reduction within the ULVZ was considered. In contrast, in recent models of coupling between mantle flow and the ULVZ, no robust microstructural models were used to predict seismic profiles (Hernlund and Jellinek, 2010; Hier-Majumder and Revenaugh, 2010). This work bridges the gap, by coupling melt redistribution with a microgeodynamic model, providing a first order prediction on the vertical variation of the seismic profile within the ULVZ.

This article presents numerical results for the transient internal structure of a partially molten column within the ULVZ, with a time-dependent mantle forcing. As outlined in Figure 1, the matrix velocity at the ULVZ-matrix interface is forced to oscillate over a range of frequencies, inducing a pulsed compaction of the ULVZ matrix. This article simulates the redistribution of both neutrally buoyant and dense interstitial melts within the ULVZ and the resultant reductions in S and P wave velocities, for five different viscosities of the ULVZ matrix. This calculation neglects the role of melt generation (Hewitt and Fowler, 2008; Rudge et al., 2011; Sramek et al., 2006) and dissolution-precipitation (King et al., 2011; Takei and Hier-Majumder, 2009). Since this calculation is carried out in a one-dimensional column, it also neglects the effect of lateral gradients of dynamic pressure arising from circulation within the ULVZ (Hernlund and Jellinek, 2010).

2. Formulation

The schematic diagram in Figure 1 outlines the problem. The domain in our formulation represents a column within the ULVZ, as depicted in the figure. The top of the column represents the mantle-ULVZ interface, and the bottom represents the CMB. When compacted, melt within this cylindrical column can migrate laterally to the other parts of the ULVZ, as if the curved wall of the cylinder is permeable. In this one dimensional model, we achieve this effect by prescribing a permeable bottom boundary, as there are no lateral boundaries to impose a permeable boundary condition. As discussed above, flow in the ambient mantle couples with the internal structure of the ULVZ through the top boundary. We impose a time dependent boundary condition for the matrix velocity at the top. Transient compaction is forced within the ULVZ layer by the transient mantle-ULVZ interface velocity. Despite the simplifications associated with the one dimensional model, this model quantifies the manner in which dynamic coupling between mantle flow and compaction within the ULVZ, modifies the spatial and temporal signature of S and P wave speeds.

2.1. Two-phase flow in the ULVZ

Consider a partially molten column within the ULVZ of height L above the CMB. Mass and momentum within this column are conserved by two coupled Partial Differential Equations (PDEs) (Bercovici et al., 2001; Hier-Majumder et al., 2006; McKenzie, 1984; Ricard et al., 2001; Richter and McKenzie, 1984). In one dimension, two PDEs – governing the conservation of mass and momentum involving the melt volume fraction $\phi(z,t)$, and the matrix velocity, $w(z,t)$ are given by

$$\frac{\partial \phi}{\partial t} = \frac{\partial}{\partial z}\left((1-\phi)w\right) \tag{1}$$

$$0 = (1-\phi)\chi^*\left(\frac{\partial \phi}{\partial z}\right) + \frac{\partial}{\partial z}\left(\mu^*\left(\frac{K_0}{\phi}+\frac{4}{3}\right)(1-\phi)\frac{\partial w}{\partial z}\right)$$

$$-(1-\phi)\Delta\rho g - \frac{c\left(w-V(t)\right)}{\phi^2}, \qquad 0 \le z \le L \tag{2}$$

where χ^* arises from the variation in surface tension with melt volume fraction (Hier-Majumder et al., 2006), μ^* is the melt fraction dependent viscosity of the matrix (Scott and Kohlstedt, 2006), K_0 is a constant $\mathcal{O}(1)$ (Bercovici et al., 2001), c is the coefficient of frictional resistance, $\Delta\rho$ is the density contrast between the ULVZ matrix and the melt, g is gravity, and $V(t) = \phi v + (1-\phi)w$, is the volume weighted average of matrix (w) and melt (v) velocities. While mass conservation of the matrix and melt phases requires V to be constant throughout the domain of the problem, it can vary with time. We choose this velocity to be the transient matrix velocity at the mantle-ULVZ interface. A consequence of this choice is that the top boundary of the domain is rendered impermeable, as discussed in detail in Appendix A.

We nondimensionalize z by L, the velocities by $\rho g/c$, and the surface tension χ^* by a constant σ/d, where σ is the grain boundary energy and d is the grain size. Following Bercovici et al. (2001), we also set $K_0 = 4/3$, leading to the nondimensional governing equations,

$$\frac{\partial \phi}{\partial t} = \frac{\partial}{\partial z}\left((1-\phi)w\right) \tag{3}$$

$$0 = \frac{(1-\phi)\chi^*}{\mathcal{B}}\frac{\partial \phi}{\partial z} + \frac{4}{3}\left(\frac{\delta}{L}\right)^2\frac{\partial}{\partial z}\left(\mu^*\frac{1-\phi^2}{\phi}\frac{\partial w}{\partial z}\right)$$

$$-R(1-\phi) - \frac{1}{\phi^2}(w - V(t)) \qquad 0 \leq z \leq 1 \tag{4}$$

where $\delta = \sqrt{\mu/c}$, is the compaction length, $R = \Delta\rho/\rho$ is the fractional density contrast between the ULVZ and the melt, and the nondimensional Bond number $\mathcal{B} = (\rho g L d)/\sigma$ is the ratio between forces arising from buoyancy and surface tension. Assuming that the melt resides in tubules along grain edges, the frictional resistance, c, depends on the grain size, d, melt viscosity μ_m, and the background melt fraction ϕ_0 by the relation (Hier-Majumder, 2011)

$$c = \mu_m \frac{72\pi}{d^2\phi_0^2}. \tag{5}$$

The quantity μ^* in equation 4 arises from melt weakening of the matrix. Currently, no direct measurement of melt weakening is available under CMB-like conditions, as the stress levels at CMB remain poorly constrained and deformation apparatus for rheological measurements under such conditions are currently unavailable. As a result, following Scott and Kohlstedt (2006), we use $\mu^* = 7\exp(-\alpha\phi)/3$, where $\alpha = 25$, even if the measurements were carried out at a confining pressure of 300 MPa. The melt fraction dependent surface tension force, χ^*, is taken from Hier-Majumder et al. (2006). In the absence of pulsation of the boundary, $V(t) = 0$, and the governing equations 3 and 4 reduce to equations 15 and 16 of Hier-Majumder et al. (2006).

The governing PDEs were solved numerically by a finite volume discretization using 500 nodes in an object oriented Fortran 2003 suite of codes. The velocity boundary conditions for the momentum equation were $w(0,t) = 0$ and $w(1,t) = V(t)$. Following the definition of $V(t)$, as demonstrated in Appendix A, the latter boundary condition renders the top of the ULVZ impermeable, an appropriate approximation for the chemically anomalous layer with a sharp boundary. The boundary condition for the melt at the top and the bottom were fixed at $\phi(0,t) = \phi(1,t) = \phi_0$, where ϕ_0 is the constant background melt fraction. Combining the velocity and melt volume fraction boundary conditions at the bottom, we notice that melt velocity in and out of the bottom boundary is given by V/ϕ_0. Since their signs are the same, during the downward motion of the top boundary, melt is expelled through the bottom, and during upward motion, melt percolates back in through the bottom boundary. The initial condition for the melt volume fraction was $\phi(z,0) = \phi_0 + \bar{\phi}(z)$, where the white noise perturbation function $\bar{\phi}(z)$ varied between 0 and 10^{-5}. At each time step, the algebraic equations resulting from discretization of the PDEs were solved using Linear Algebra PACKage (LAPACK) routines available through intel Math Kernel Library. Once the solution for matrix velocities were obtained, the melt fraction was updated by integrating the mass conservation equation 3 in time using the Courant criterion. The numerical solutions compare well with analytical solutions available for simple cases. One such analytical solution, following the models of forced compaction by Ricard et al. (2001) is compared against the numerical solutions for matrix and segregation velocities in Appendix B. In Appendix B, we also report the methods and results from a series of numerical experiments testing the resolution of the model with respect to grid size.

The characteristic length scale L is 20 km. Five different values of the matrix viscosity ranging between 10^{20} and 10^{24} Pas were used in the simulation. The nondimensional constant R was set to 0 and -0.03 for the two different cases. The volume averaged boundary velocity was prescribed as

$V(t) = 2\pi\omega V_0 \sin(2\pi\omega t)$. A set of numerical experiments for four different ordinary frequencies of pulsation 1×10^{-2}, 6.6×10^{-3}, 3.3×10^{-3}, and 1×10^{-3}, were carried out. The dimensional time periods corresponding to these frequencies range between 0.1 and 1 Ma. The dimensionless amplitude of the oscillation was fixed at $V_0 = -5\times10^{-3}$. Values of all dimensional constants and nondimensional numbers are provided in Table 1.

2.2. Calculation of seismic velocities

Two groups of parameters determine the seismic signature of partially molten rocks. The first group involves the elastic moduli and density of the matrix and the melt. The second group of parameters arise from the volume fraction and grain-scale distribution of melt. The second group of parameters are represented by contiguity, the fractional area of intergranular contact (Hier-Majumder, 2008; Park and Yoon, 1985; Takei, 1998, 2002). Contiguity in a partially molten aggregate depends strongly on melt volume fraction (von Bargen and Waff, 1986; Wimert and Hier-Majumder, 2012) and modestly on the wetting angle (Hier-Majumder and Abbott, 2010). Wetting angles under ULVZ-like conditions are currently unconstrained. This work, therefore, ignores the influence of wetting angle and focuses on the first order influence of melt volume fraction on the seismic signature.

For the matrix, we use bulk and shear moduli and Poisson's ratio from the PREM model under CMB condition. For the melt phase, we determined the bulk modulus of a peridotite melt using the Vinet equation of state based on data from Guillot and Sator (2007). While the presence of Fe-rich solids likely reduce the effective bulk and shear moduli of the ULVZ (Mao et al., 2006; Wicks et al., 2010), the extent of reduction depends on the volume fraction of these solids (Wimert and Hier-Majumder, 2012), which is unknown. To reduce the uncertainty, we prescribed PREM-like elastic properties to the ULVZ matrix. The calculated seismic velocity reductions, therefore, provide only upper limits. If the presence of Fe-rich solids are accounted for, less melt volume fraction will be necessary to generate the seismic signature. See Wimert and Hier-Majumder (2012) for discussions on this trade-off and the relatively small influence of variations in the melt bulk modulus on the seismic signature.

Contiguity at each point within the ULVZ was calculated from the melt volume fraction using the parameterization from Wimert and Hier-Majumder (2012). In their microstructural model, the melt resides in tubules. As the melt fraction increases, the area of cross section of melt tubules increase and intergranular contacts are wetted, reducing the contiguity. The relation between contiguity, ψ, and melt fraction, ϕ, is given by the polynomial function

$$\psi = -8065\phi^5 + 6149\phi^4 - 1778\phi^3 + 249\phi^2 - 19.77\phi + 1, \tag{6}$$

where $0 \leq \phi \leq 0.25$.

Relative S and P wave velocities, V_S/V_0^S and V_P/V_0^P, were calculated by using the 'equilibrium geometry' model of Takei (2002). In this model, the quantities are expressed as functions of effective elastic moduli and density,

$$\frac{V_S}{V_0^S} = \sqrt{\frac{(N/G)}{(\bar{\rho}/\rho)}}, \tag{7}$$

and

$$\frac{V_P}{V_0^P} = \sqrt{\frac{K_e/K + 4\beta/3\,(N/G)}{(1+4\beta/3)\,(\bar{\rho}/\rho)}}, \tag{8}$$

where K, G, and ρ are the bulk modulus, shear modulus, and density of the solid, and $\beta = G/K$. The quantity $\bar{\rho}$ is the volume averaged density of the aggregate. The quantity N is the shear modulus of the intergranular skeletal framework and K_e is the effective bulk modulus of the grain-melt aggregate.

The effective elastic moduli of the partially molten aggregate can be expressed in terms of contiguity ψ and the elastic moduli of the solid and the melt as

$$
\begin{aligned}
N &= G\,(1-\phi)\,g(\psi) && (9)\\
K_e &= K\left[(1-\phi)h(\psi) + \frac{(1-(1-\phi)h(\psi))^2}{(1-\phi)(1-h(\psi)) + \phi K/K_m}\right], && (10)
\end{aligned}
$$

where K_m is the bulk modulus of the melt, and the functions $g(\psi)$ and $h(\psi)$ are given by,

$$
\begin{aligned}
g(\psi) &= 1-(1-\psi)^n, && (11)\\
h(\psi) &= 1-(1-\psi)^m, && (12)
\end{aligned}
$$

where the exponents n and m depend on the contiguity, ψ, and Poisson's ratio, ν (Takei, 2002, App. A).

At each time step of the numerical solution, the melt distribution within the ULVZ is determined by solving the coupled mass and momentum conservation equations 3 and 4. Then, the parameterization in equation 6 was used to evaluate the contiguity at each point within the ULVZ. Knowing the contiguity, ψ, the effective elastic moduli in equations 9 and 10 were evaluated, which were subsequently used to evaluate V_S/V_0^S and V_P/V_0^P from equations 7 and 8, respectively.

3. Results

The transient internal structure of the ULVZ depends strongly on transient forcing from mantle flow, density contrast between the melt and ULVZ matrix, and the viscosity of the ULVZ matrix. The seismic signature varies spatially and temporally within the ULVZ differently for different melt densities. Distribution of neutrally buoyant melts are more strongly influenced by pulsed compaction. These results are discussed in detail below.

3.1. Numerical solution

3.1.1. Internal structure of the ULVZ

Pulsed compaction redistributes the neutrally buoyant melt within the ULVZ, leading to a periodic oscillation in the spatially varying seismic signature. The series of plots in Figure 2 outline the melt distribution ϕ, matrix velocity, w, and the relative S and P wave velocities, V_S/V_0^S and V_P/V_0^P, respectively. The plot in Figure 2(a) depicts a narrow, melt-rich, decompaction layer that forms near the top and a broad compacted, melt-poor region that forms near the bottom during the downward motion of the boundary. The matrix velocities in Figure 2(b) are negative throughout the column during the downward motion and change sign during the upward motion of the mantle-ULVZ interface. As the melt-rich layer forms near the top, to conserve mass, the matrix collects near the bottom, illustrated by the downward, negative matrix velocity. Comparison between the melt fraction and velocity profiles for the case B in Figures 2(a) and (b) indicates a delay between the imposition of the maximum negative matrix velocity and formation of the decompaction layer at the top. The legends on the curve in this panel indicate the time steps in a given cycle, annotated in Figure 4. Viscosity of the ULVZ matrix is 10^{20} Pas for these simulations.

The seismic velocities within the ULVZ column reflect the spatial and temporal variations in melt volume fraction. As a result of melt redistribution, calculated values of V_S/V_0^S and V_P/V_0^P, in Figure 2(c) and (d) display a sharp drop near the top and a gradual increase towards the bottom following periods of downward motion of the boundary.

In contrast to the neutrally-buoyant melt, the dense melt percolates down the matrix, generating a melt-rich layer near the bottom of the column and a compaction layer near the top, as illustrated in Figure 3(a). Similar to Figure 2, the matrix velocity distribution within the ULVZ is forced by the prescribed velocity at the ULVZ-matrix interface, as demonstrated in panel (b). The legends on the curves in panel (b) correspond to the same times as in Figure 2(b). Notice that the magnitude of the decompaction layer in panel (a) is much smaller than the magnitude of the decompaction layer in panel (a) of Figure 2. The seismic signature within the ULVZ, depicted in Figures 3(c) and (d) display a decrease in S and P wave velocities from under the decompaction layer to the bottom of the ULVZ. The matrix viscosity for these simulations is also 10^{20} Pas.

Both of the above cases illustrate variations in the melt distribution along the entire depth of the ULVZ with time. Evolution of the internal structure of ULVZ, discussed above, was confined within one cycle of topographic oscillation. In the following section, we take a look at the variation of melt volume fraction and the resulting seismic signature near the top and the bottom of the ULVZ over the length of several cycles of pulsed compaction.

3.1.2. Melt redistribution with time

The internal structure of the ULVZ and the resultant seismic signature respond to the pulsation of ULVZ topography depending on the density contrast between the melt and the matrix. This section presents results on temporal variation for a matrix viscosity of 10^{20} Pas.

The series of plots in Figure 4 illustrates the coupling between pulsed compaction and melt redistribution within the layer. Dimensional velocity of the top of the ULVZ layer, V, is plotted as a function of time in Figure 4(a). A negative value of V implies periods of compaction of the ULVZ, as the mantle flow exerts a compression on the ULVZ through the mantle-ULVZ interface. Over several hundred ka, evolution of the average melt volume fraction within the ULVZ depends strongly on the density contrast between the melt and the matrix. The locally averaged melt volume fraction from the top and bottom 400 m are plotted as functions of time in Figures 4(b) and (c), respectively. The top decompaction layer develops following the downward displacement of the top boundary. The average melt fraction in this layer reaches a maximum as the imposed velocity becomes zero and returns to the unperturbed state during the upward motion of the boundary. The magnitude of this oscillation is independent of the frequency of the forced pulsation of the topography. Even as the amplitude of the mantle-ULVZ interface velocity is different for different frequencies, the amplitude of the average melt volume fraction curves are insensitive to these variations. The rate of growth and decay of the decompaction and compaction layers, however, depend on the magnitude and frequency of the oscillations in the ULVZ-mantle interface velocity.

Redistribution of dense melts follow a distinct trend. The set of curves marked with $\Delta\rho = -3\%$, in Figures 4(b) and (c) illustrate this trend. The dense melt drains from the top and collects at the bottom, changing the corresponding local averages. While these averages change over several hundred ka, high frequency oscillations in the melt volume fractions are still apparent from some of the curves. Over short period of times, melt redistribution arising from such high frequency oscillations also display the formation of a melt-rich layer near the top and a compacted layer near the bottom. Over geologic timescales, however, the effect of buoyancy dominates over the effect of topographic oscillation.

The seismic signature arising from a neutrally buoyant melt oscillates about a mean value, as depicted in Figure 5(a)–(d). During periods of compaction, the top 400 m of the ULVZ records up to 25% reduction in S wave speed, while the bottom 400 m records only 5% reduction at the same time. At times when the topography of the ULVZ returns to its initial state, both the top and the bottom of the ULVZ record an average reduction of 15% in the S wave velocities. A similar oscillatory behavior is observed for P wave velocities, where the magnitude of variation is much smaller, but follows the oscillation of the compaction. For all four frequencies tested in this work, the amplitude of the oscillatory seismic signal is independent of the frequency of topographic pulsation.

The seismic signature arising from a melt denser than the ULVZ is distinct from a neutrally buoyant melt. The series of plots in Figure 6(a)–(d) depict the variations in of V_S/V_0^S and V_P/V_0^P in the top and bottom 400 m of the ULVZ. As melt drains out from the top and pools near the bottom, the average S wave speed increases near the top and decreases near the bottom. High frequency pulsations lead to some damped oscillation in the seismic signals. Over 350 ka, however, gravitational drainage dominates the seismic signature. Over this time, the decrease in S wave speed near the top is less

(5–10%) compared to the decrease in the S wave speed near the bottom (15–20%), as depicted in Figures 6 (a) and (b). The decrease in S wave speed near the bottom depends on the rate of melt drainage from the top of the column to the bottom. A higher initial melt fraction will reduce the frictional resistance to melt percolation and accelerate melt drainage (Hier-Majumder, 2011; Hier-Majumder and Courtier, 2011), while a stronger surface tension will reduce the drainage efficiency (Hier-Majumder et al., 2006). Similar to the S wave speed reduction, the P wave speed reduction near the top is also smaller than the bottom.

3.1.3. The role of matrix viscosity

Melt redistribution near the top and the bottom of the ULVZ is strongly modulated by the matrix viscosity. The plot in Figure 7(a) compares the melt redistribution near the top 400 m for two different matrix viscosities. The amplitude and frequency of oscillation of the ULVZ-mantle interface velocity is the same for both curves. Despite the same amount of forcing from the mantle, the peak magnitude of the decompaction layer is substantially smaller for higher matrix viscosity. The plot in Figure 7(b) compares the peak magnitude of the decompaction layer, melt volume fraction over the top 400 m, for five different matrix viscosities. The magnitude of the decompaction layer drastically decreases for matrix viscosities exceeding 10^{21} Pas, when the top melt fraction is nearly indistinguishable from the background melt volume fraction of 0.05.

High matrix viscosity increases the compaction length of the layer. As the top axis in Figure 7(b) indicates, the compaction length, δ is more than an order of magnitude higher than the ULVZ height for a matrix viscosity of 10^{22}

Pas. For such large compaction lengths, melt segregation due to compaction is rendered inefficient over ULVZ-like length scales. Based on the scaling between ULVZ topography and viscosity, Hier-Majumder and Revenaugh (2010) suggest that the typical viscosity of the ULVZ should vary between 10^{19} Pas and 10^{20} Pas. For such values of the ULVZ matrix viscosity, the effect of compaction should be pronounced, as suggested by the plot in Figure 7(b). The qualitative behavior of melt segregation in this case is similar to the mesoscale experiments carried out by Holtzman et al. (2003).

3.2. Analytical Solution

Analysis of the governing nonlinear PDEs provide us with a wealth of information regarding the behavior of the solutions. In the absence of density contrast between the melt and the matrix, growth and decay of the decompaction layers are driven by the imposed velocity V. In this section, we present a nonlinear analysis outlining the way such a growth rate depends on the imposed velocity, V and the melt volume fraction.

We seek a solution to the governing mass and momentum conservation equations 3 and 4, respectively. This system of PDEs can be combined to yield a nonlinear, dispersive, and dissipative wave equation in melt volume fraction (Barcilon and Lovera, 1989; Hier-Majumder et al., 2006; Rabinowicz et al., 2002; Spiegelman, 1993). Following Hier-Majumder et al. (2006), we seek a solution for the melt volume fraction ϕ in terms of a similarity variable $f = z - w_0 t$, where w_0 is a reference velocity, such that,

$$\phi = \phi(f). \tag{13}$$

In the following analysis, we neglect the effect of surface tension and buoyancy. We also set $\mu^* = 1$ in equation 4. We integrate the mass conservation equation once to obtain,

$$w = -\frac{w_0\phi + K_1}{1-\phi}, \tag{14}$$

where K_1 is a constant of integration. Substituting w into the nondimensional momentum conservation equation 4, we convert it into an ODE in $\phi(f)$, given by,

$$0 = -\frac{4}{3}\left(\frac{\delta}{L}\right)^2 (w_0 + K_1)\left(\frac{1+\phi}{\phi\,(1-\phi)}\phi'\right)' + \frac{1}{\phi^2}\left(\frac{w_0\phi + K_1}{1-\phi} + V\right), \tag{15}$$

where the primes indicate differentiation with respect to f. Following the analysis outlined by Rabinowicz et al. (2002), we assume that far from the peak of the solution, the melt volume fraction assumes a constant background value $\phi = \phi_0$. This condition requires that both the gradient and the curvature of the solution vanishes such that $\phi' = \phi'' = 0$ at $\phi = \phi_0$. Inserting this boundary condition into the ODE 15 leads to

$$K_1 = -\left(w_0\phi_0 + (1-\phi_0)V\right). \tag{16}$$

This constant of integration is the volume averaged velocity of the melt and the matrix. Inserting K_1 into 15, multiplying by an integrating factor, and integrating once we get

$$\frac{4}{3}\left(\frac{\delta}{L}\right)^2 \frac{(1+\phi)^2\,(1-\phi_0)}{\phi^2\,(1-\phi)^2}\,(\phi')^2 = g(\phi) - \frac{K_2}{w_0 - V} \tag{17}$$

where K_2 is the second constant of integration and the function $g(\phi)$ is given as,

$$g(\phi) = \frac{\phi_0}{\phi^2} - \frac{2\,(1-3\phi_0)}{\phi} + 2\,(3-5\phi_0)\ln\left(\frac{\phi}{1-\phi}\right) + \frac{4\,(1-\phi_0)}{1-\phi}. \tag{18}$$

Once again, imposing $\phi' = 0$ at $\phi = \phi_0$, and solving for K_2, we can rewrite equation 17 as,

$$\phi' = \pm \left(\frac{L}{\delta}\right) \frac{\phi\,(1-\phi)}{1+\phi} \sqrt{\frac{3}{4}\left(\frac{g(\phi) - g(\phi_0)}{1-\phi_0}\right)}. \tag{19}$$

In the limit of small melt fraction, $\phi \ll 1$, we can ignore the first term in the compaction rate, $\partial((1-\phi)w)/\partial z$, and rewrite the mass conservation equation 4 as,

$$\frac{\partial \phi}{\partial t} \approx \frac{\partial w}{\partial z} = \mp\,(w_0 - V)\left(\frac{L}{\delta}\right) \frac{\phi}{1-\phi^2} \sqrt{\frac{3}{4}\,(g(\phi) - g(\phi_0))\,(1-\phi_0)}, \tag{20}$$

which is linear in V and inversely related to the compaction length. The normalized magnitude of compaction rate, $|(\partial w/\partial z)/(w_0 - V)|$ from equation 20 depends on both the compaction length and the background melt fraction. While this normalized compaction rate at any point within the ULVZ increases with the melt fraction at that point, the rate of increase is modified by both the compaction length and the background, initial melt fraction. As the series of curves in Figure 8(a) indicate, the compaction rate is higher for smaller compaction lengths, as indicated by the inverse relationship of $|(\partial w/\partial z)/(w_0 - V)|$ with compaction length in equation 20. For a given compaction length, as the series of curves in Figure 8(b) indicates, the magnitude of the growth rate is higher for a smaller background melt fraction. In other words, decompaction layers will develop faster in response to a forcing in a ULVZ with a smaller background melt fraction.

4. Discussions

This article models internal melt redistribution within the ULVZ for both the dense and neutrally buoyant melts. Based on seismic observations of

ULVZ density (Rost et al., 2006), a neutrally buoyant melt in an Fe-rich matrix is likely a better approximation to the ULVZ. The excess density of the ULVZ cannot be explained only by melting while satisfying the seismic observations and geodynamic models. For example, if the ULVZ matrix has a density similar to PREM, then for an average melt volume fraction of 0.05, the melt has to be 3 times denser than a PREM-like solid to explain the observed 10% higher density of the ULVZ. Preserving an interconnected melt of such high density within the ULVZ over geologic times is physically untenable.

Mantle convection, through pulsed compaction, redistributes neutrally buoyant melt within a partially molten ULVZ. A few important implications of this phenomenon involve: 1. larger speed reduction near the top of the ULVZ; 2. vertical variation of seismic speed reduction that does not require a variation in the melt microstructure; and 3. spatial variation of the magnitude of speed drop associated with ULVZs. Each of these issues are discussed below.

1. Melt distribution within the ULVZ is rarely uniform. Especially, if the dense ULVZ matrix contains an equally dense partial melt, during periods of downward motion of the ULVZ-mantle interface, wave speed reductions will be much larger near the top of the ULVZ. *If the overall seismic signature for a ULVZ patch is dominated by the signature at the top, the inferred melt volume can be larger than the average melt volume fraction in the ULVZ.*
2. Vertical variation of seismic structure within the ULVZ can be a consequence of pulsed compaction or stirring. To explain such observed

variations, Rost et al. (2006) suggested that the melt geometry changes from tubules near the top to spherical inclusions near the bottom of the ULVZ. The mechanism driving such microstructural changes, however, is not clear. This article employed the contiguity-melt volume fraction parametrization of Wimert and Hier-Majumder (2012), to calculate the seismic speed reductions. In their microgeodynamic model, melt resides within grain edge tubules through the entire range of melt volume fractions of interest. *It is, therefore, not necessary to invoke variation of melt microstructure to explain the vertical variation in seismic signature.*

3. Signature of ULVZ patches atop the CMB vary spatially (McNamara et al., 2010; Rost et al., 2010). Previous dynamic models indicate that the topography of the ULVZ depends on the nature of the ambient mantle flow (Bower et al., 2011; Hier-Majumder and Revenaugh, 2010; McNamara et al., 2010). Additionally, *the result from this work indicates that the magnitude of speed reduction within a ULVZ patch can also be controlled by ambient mantle flow through pulsed compaction.* To fully understand the nature of the ULVZ, it is therefore, crucial to understand the nature of the flow in the surrounding mantle.

A few issues need to be investigated in greater detail. First, this work needs to be extended into higher dimensions to investigates the role of lateral pressure gradients and various patterns of ambient mantle flow. Secondly, this isothermal calculation starts with an initial homogeneous melt distribution. The bottom of the ULVZ is warmer, and likely subject to a larger amount of melt compared to the top. The implications for melt redistribu-

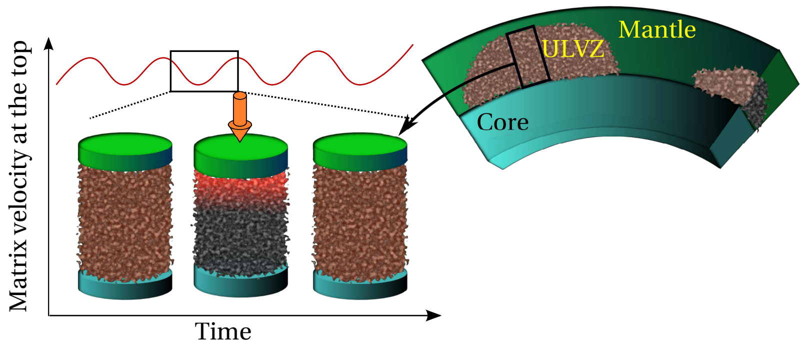

Figure 1: A schematic diagram outlining the geometry of the problem. A periodic forcing of the partially molten column redistributes the melt within the column.

tion and the seismic signature under such conditions need to be considered. In addition, measurements of solidus temperatures for a variety of melt compositions and tighter estimates on the CMB temperature are also required.

Acknowledgments

This work was supported by the NSF grant EAR0911094. Insightful comments and suggestions from Yannick Ricard, Dave Bercovici, Allen McNamara, John Rudge, Sebastian Rost, and an anonymous reviewer is greatly appreciated. Insightful reviews and comments from Cian Wilson, Mark Jellinek, and two anonymous reviewers greatly helped the second version of the manuscript.

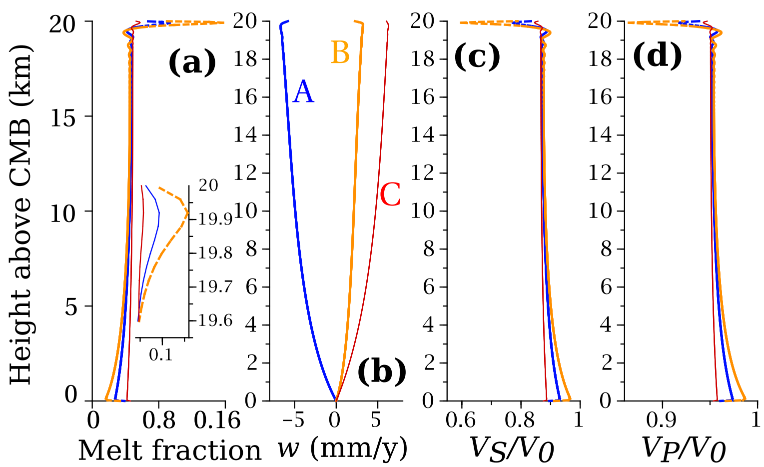

Figure 2: Internal structure and seismic signature of the ULVZ containing a neutrally buoyant melt. The vertical axis in all panels indicate the height of the ULVZ in km. (a) Melt volume fraction, (b) matrix velocity in mm/y, (c) relative S wave speed and (d) relative P wave speed for three different time steps. The legends in (b) correspond to three different stages during a compaction cycle, annotated in Figure 4(a), and apply for all panels. The inset in panel (a) displays the evolution of melt volume fraction for in the top 400 m of the ULVZ, corresponding to the three stages of the compaction cycle. The simulation corresponds to a nondimensional frequency of pulsation $\omega = 0.01$.

Symbol	Quantity	Value	Unit
ϕ_0	Background melt fraction	0.05	
R	Fractional density contrast	-0.03, 0.00	
$\mathcal{B}$	Bond number	1.20×10^6	
ρ	Matrix density	5600.00	kgm^{-3}
g	Gravity	10.70	ms^{-2}
σ	Surface tension	1.00	Jm^{-2}
d	Grain size	1.00×10^{-3}	m
c	Frictional resistance	9.04×10^{10}	Pasm^{-2}
μ	Matrix viscosity	$10^{20}, 10^{21}, 10^{22}$	
		$10^{23}, 10^{24}$	Pas
L	Length scale	20.00×10^3	m
v_0	Characteristic velocity	6.62×10^{-7}	ms^{-1}
δ	Compaction length	33.25, 105.13, 332.5	
		1051.3, 3324.5	km
K	Matrix bulk modulus	655.60	GPa
G	Matrix shear modulus	293.80	GPa
K_m	Melt bulk modulus	583.44	GPa
ν	Matrix Poisson's ratio	0.31	
w_0	Reference velocity		ms^{-1}

Table 1: Constants used in the calculation.

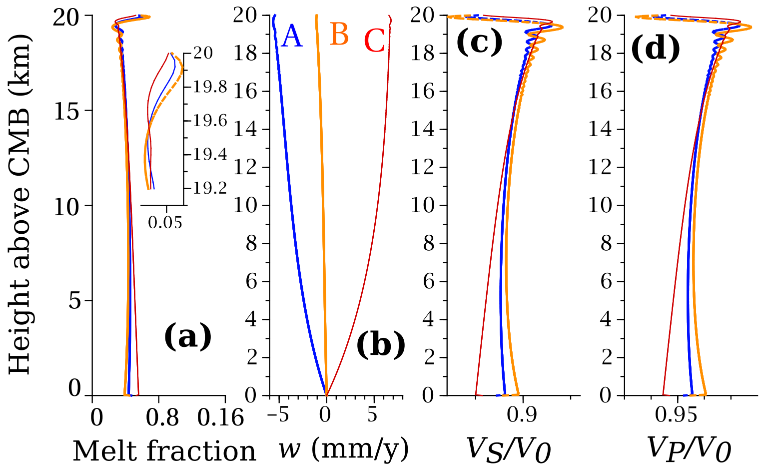

Figure 3: Internal structure and seismic signature within the ULVZ containing a melt 3% denser than the matrix. The quantities in all subfigures are similar to Figure 2. This set of simulations also correspond to a nondimensional frequency of oscillation, $\omega = 0.01$.

Appendix A. Derivation of the governing equations

In a partially molten, viscous aggregate, melt distribution is coupled through matrix and melt velocities by a set of coupled governing equations. If the velocities of the melt and the matrix phase are given as $\boldsymbol{v}$ and $\boldsymbol{w}$, then, in the absence of melt generation and dissolution precipitation, conservation of the melt and matrix mass is given by

$$0 = \frac{\partial \phi}{\partial t} + \boldsymbol{\nabla} \cdot (\phi \boldsymbol{v}), \tag{A.1}$$

and

$$\frac{\partial \phi}{\partial t} = \boldsymbol{\nabla} \cdot ((1-\phi)\boldsymbol{w}). \tag{A.2}$$

Since the viscosity of the melt is many orders of magnitude smaller than that of the matrix, we ignore the viscous stresses in the melt phase, leading to the

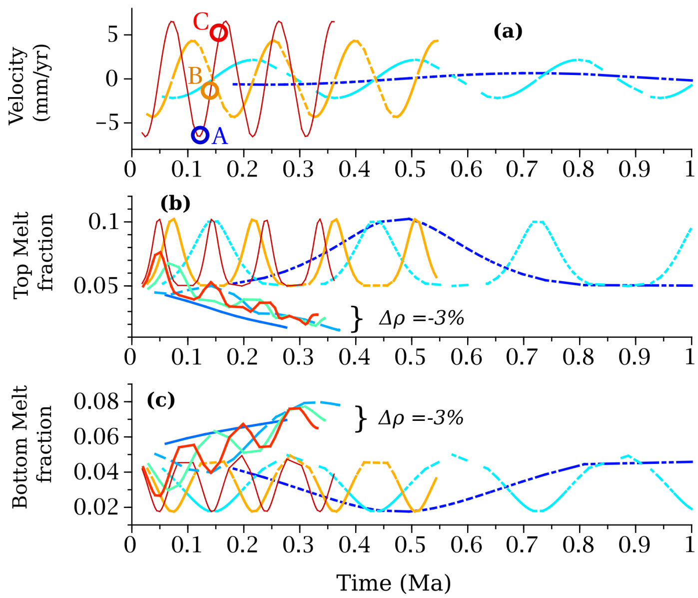

Figure 4: Transient mantle-ULVZ interfacial velocity and melt fractions within the ULVZ. The different curves correspond to four different frequencies. (a) Velocity of the ULVZ-mantle interface, as a function of time for the four different frequencies. Annotations in panel (a) correspond to the three time steps for which the vertical profiles are displayed in Figures 2 and 3. (b) Melt volume fraction averaged over the top 400 m of the ULVZ as a function of time. The plots are depicted only for the first 1 Ma. (c) Melt volume fraction averaged over the bottom 400 m of the ULVZ as a function of time in Ma.

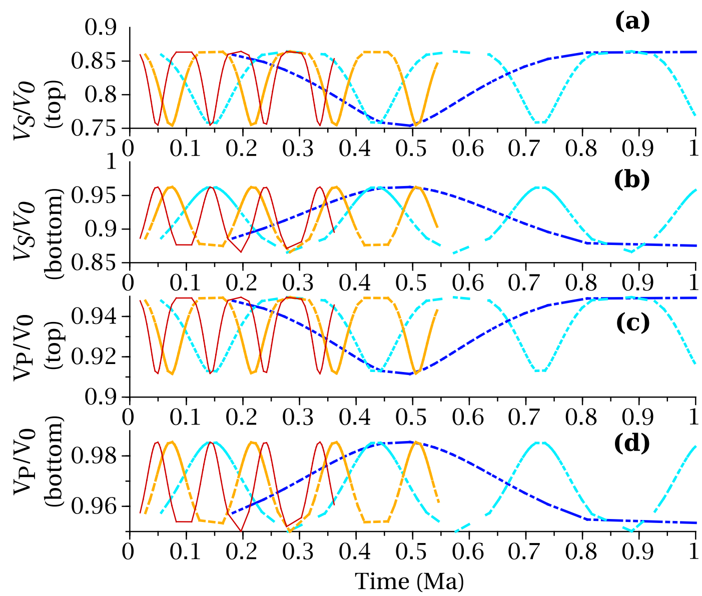

Figure 5: Transient seismic signature within the ULVZ. Relative reductions in S wave velocities near the (a) top and (b) bottom 400 m are plotted as a function of time for 4 different frequencies of pulsed compaction. The plots in Figure (c) and (d) depict the relative drops in P wave speed for the same regions within the ULVZ. In these plots, density of the melt is equal to the density of the matrix.

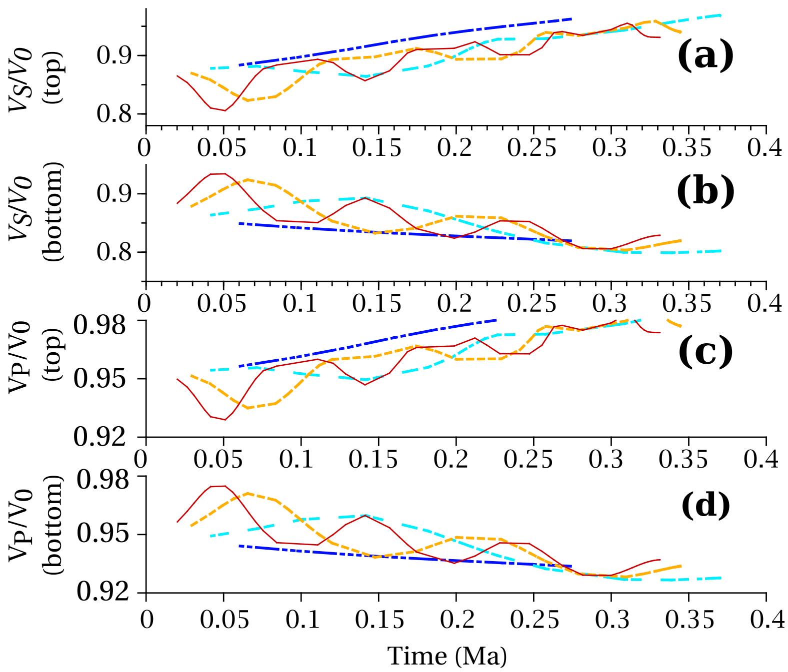

Figure 6: Transient seismic signature within the ULVZ. The physical parameters are similar to Figure 5, except for the melt density. In these plots, the melt is 3% denser than the ULVZ matrix. Relative reductions in S wave velocities near the (a) top and (b) bottom 400 m are plotted as a function of time for 4 different frequencies of pulsed compaction. The plots in Figure (c) and (d) depict the relative drops in P wave speed for the same regions within the ULVZ.

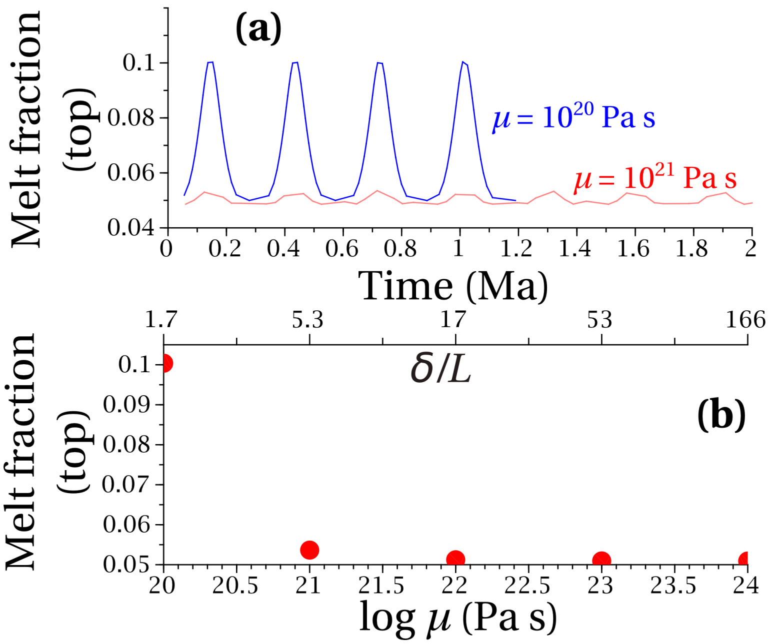

Figure 7: Role of matrix viscosity on the magnitude of the decompaction layer. (a) Plot of the averaged melt volume fraction over the top 400 m as a function of time for two different matrix viscosities, annotated next to the curves. (b) Highest magnitude of the decompaction layer as a function of logarithm of matrix viscosity. The axis on the top depicts the ratio between compaction length and the thickness of the ULVZ.

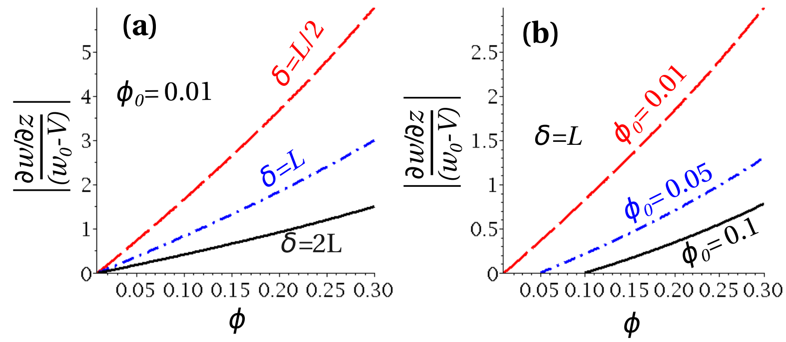

Figure 8: Plot of the magnitude of strain rate, $|(\partial w/\partial z)/(w_0 - V)|$, as a function of melt volume fraction, ϕ, for different values of (a) compaction length and (b) background melt fraction, ϕ_0. The annotations on the curves represent the value of the parameter. All curves in (a) correspond to $\phi_0 = 0.01$, and all curves in (b) correspond to $\delta = L$.

coupled conservation equations,

$$0 = -\phi\left(\boldsymbol{\nabla} P_m + \rho_m \boldsymbol{g}\right) + c(\boldsymbol{w} - \boldsymbol{v}), \tag{A.3}$$

and

$$\begin{aligned} 0 = & -(1-\phi)\left(\boldsymbol{\nabla} P + \rho \boldsymbol{g}\right) - c(\boldsymbol{w} - \boldsymbol{v}) + \boldsymbol{\nabla}\cdot((1-\phi)\mathbf{T}) \\ & + (\chi + P - P_m)\boldsymbol{\nabla}\phi, \end{aligned} \tag{A.4}$$

where P_m is the melt pressure, P is the matrix pressure, ρ_m is the melt density, ρ is the matrix density, c is the frictional resistance to melt percolation, χ is the surface tension force per unit area, and the matrix stress $\mathbf{T}$ is given by the constitutive relation,

$$\mathbf{T} = \mu\left(\boldsymbol{\nabla}\boldsymbol{w} + (\boldsymbol{\nabla}\boldsymbol{w})^T - \frac{2}{3}(\boldsymbol{\nabla}\cdot\boldsymbol{w}) \quad \mathbf{I}\right), \tag{A.5}$$

where μ is the viscosity of the matrix and $\mathbf{I}$ is the unit tensor. In addition to the above relations, we need an extra closure relation between the melt and the matrix pressure, given by,

$$\chi + P - P_m = -\frac{K_0 \mu}{\phi(1-\phi)}\left(\frac{\partial \phi}{\partial t} + \boldsymbol{w}\cdot\boldsymbol{\nabla}\phi\right), \tag{A.6}$$

where K_0 is a constant $\mathcal{O}(1)$.

To obtain the one-dimensional governing equations, we first add the mass conservation equations A.1 and A.2 to obtain,

$$\frac{\partial}{\partial z}\left(\phi v + (1-\phi) w\right) = 0, \tag{A.7}$$

which implies the volume averaged velocity $\phi v + (1-\phi)w$ is constant throughout the domain of calculation. We prescribe,

$$\phi v + (1-\phi) w = V, \tag{A.8}$$

where V is the volume averaged velocity of the aggregate, which we also set as the velocity of the ULVZ-mantle interface.

Next, we eliminate the pressure and melt velocity from the momentum equations multiplying equation A.3 by $(1-\phi)$ and equation A.4 by ϕ, adding, and substituting the stress, pressures, and melt velocity from equations A.5, A.6, and A.8, to obtain the one-dimensional action-reaction equation,

$$\begin{aligned} 0 \;\;=\;\; & (1-\phi)\chi^* \frac{\partial \phi}{\partial z} + \frac{\partial}{\partial z}\left(\mu\left(\frac{K_0}{\phi} + \frac{4}{3}\right)(1-\phi)\frac{\partial w}{\partial z}\right) \\ & -(1-\phi)\Delta\rho g - \frac{c\,(w - V)}{\phi^2}, \end{aligned} \tag{A.9}$$

where $\chi^* = (\mathrm{d}\chi)/(\mathrm{d}\phi)$.

Thus we have two partial differential equations, A.2 and A.9 on two unknowns ϕ and w. First, we impose the impermeability condition at the top boundary $z = h$ such that

$$v|_{z=h} = w|_{z=h}\,, \tag{A.10}$$

implying $w = V$ at $z = h$.

Besides the impermeable boundary condition at the top, given by equation A.10, we also impose zero velocity of the matrix at the bottom boundary. We prescribe the initial melt distribution, given by,

$$\phi(z, 0) = \phi_0 + \bar{\phi}(z), \tag{A.11}$$

where the white noise perturbation $\bar{\phi}(z)$, varies between 0 and 10^{-5}. The small white noise is necessary to ensure small, but nonzero gradients in melt volume fraction, which allows time marching of the numerical solutions.

Appendix B. Analytical solution for initial matrix velocity

In the limit of a negligibly small increment in time from the beginning, the mass and momentum conservation equations admit a simple analytical solution, which can be compared with the numerical solution. The analytical solutions presented here follow the forced compaction model of Ricard et al. (2001).

Immediately after the beginning of the simulation, we assume that the melt distribution is very similar to the original melt distribution. The assumption applies in the limit $t \to 0$, $\partial\phi/\partial z \to 0$. In the absence of surface tension, the nondimensional momentum conservation equation then reduces to the Ordinary Differential Equation (ODE) in matrix velocity w, given by,

$$0 = \frac{4}{3}\left(\frac{\delta}{L}\right)^2 \mu^* \frac{1-\phi^2}{\phi}\left(\frac{\mathrm{d}^2\bar{w}}{\mathrm{d}z^2}\right) - R(1-\phi) - \frac{1}{\phi^2}\left(\bar{w} - V(t)\right) \tag{B.1}$$

We set $\mu^* = 1$, substitute $z = z_0 y$ and $\bar{v} = R\phi^2(1-\phi) - V + \bar{w}$ where,

$$z_0 = \left(\frac{\delta}{L}\right)\sqrt{\frac{4\phi}{3}\left(1-\phi^2\right)}. \tag{B.2}$$

This substitution reduces the ODE B.1 to

$$\frac{\mathrm{d}^2\bar{v}}{\mathrm{d}y^2} - \bar{v} = 0, \tag{B.3}$$

A general solution, similar to Ricard et al. (2001) to equation B.3, is given by,

$$\bar{v} = A\cosh y + B\sinh y. \tag{B.4}$$

We set the boundary conditions $\bar{w}(0,t) = 0$ and $\bar{w}(1,t) = V(t)$, and substitute into equation B.3 to obtain the constants,

$$A = R\phi^2(1-\phi) - V \tag{B.5}$$

$$B = \frac{R\phi^2(1-\phi)\left[1-\cosh\left(\frac{1}{z_0}\right)\right] + V\cosh\left(\frac{1}{z_0}\right)}{\sinh\left(\frac{1}{z_0}\right)}. \tag{B.6}$$

The analytical solution for the matrix velocity, $\bar{w}$ and the segregation velocity, $\Delta V = (\bar{w}-V)/\phi$, is displayed in Figure B.1 for a constant $\phi = 0.05$. Overlain on the plot is also the numerical solution for $\phi = 0.05$ at time 0.

A number of numerical experiments were carried out to test the influence of grid resolution on the results. First, we define the residual vector

$$\boldsymbol{\epsilon} = \bar{\boldsymbol{w}} - \boldsymbol{w}, \tag{B.7}$$

where $\bar{\boldsymbol{w}}$ is the analytical solution and $\boldsymbol{w}$ is the numerical solution. As a measure of convergence of the solution, we define the L_∞ norm or the largest absolute value of the residual vector within the top 1 km of the ULVZ as,

$$||\boldsymbol{\epsilon}||_\infty = \max|\epsilon_i|,\ 1 < i < n_{top} \tag{B.8}$$

where the range of the index i spans over the top 1 km of the ULVZ. We calculate the norm $||\boldsymbol{\epsilon}||_\infty$ for a number of grid sizes ranging between 50 and

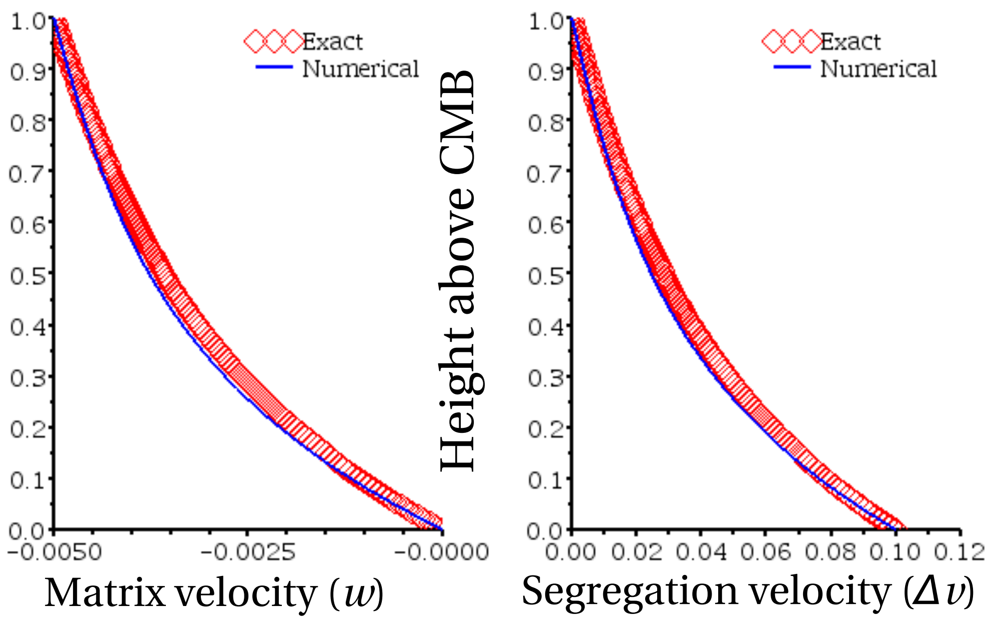

Figure B.1: Analytical solutions for nondimensional matrix and segregation velocities in open diamonds are compared with the numerical solution at time 0 . In this calculation $V = -0.005$

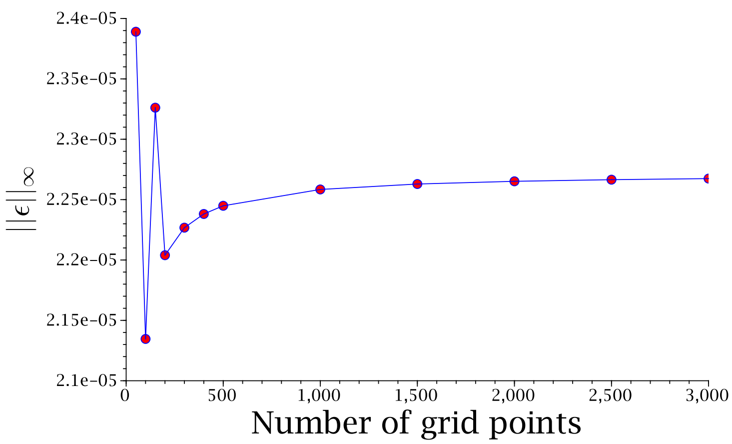

Figure B.2: A plot of the L_∞ norm of the error vector ϵ over the top 1 km of the ULVZ, as a function of the grid size. .

3000. The result is plotted in Figure B.2. The error oscillates about a value of $\sim 2.25 \times 10^{-5}$ for grids sizes smaller than 500. The oscillations in the value of the error for such low resolution grids is typically $\mathcal{O}(10^{-6})$, which corresponds to approximately 0.4% of the absolute maximum of $\boldsymbol{w}$ within the top 1 km of the ULVZ.

References

Barcilon, V., Lovera, O., 1989. Solitary waves in magma dynamics. Journal of Fluid Mechanics 204, 121–133.

Bercovici, D., Ricard, Y., Schubert, G., 2001. A two-phase model for compaction and damage; 1, General theory. Journal of Geophysical Research, B, Solid Earth and Planets 106 (5), 8887–8906.

Bower, D. J., Wicks, J. K., Gurnis, M., Jackson, J. M., 2011. A geodynamic and mineral physics model of a solid-state ultralow-velocity zone. Earth and Planetary Science Letters 303 (3-4), 193 – 202.
URL http://www.sciencedirect.com/science/article/pii/S0012821X10008083

Fiquet, G., Auzende, A. L., Siebert, J., Corgne, A., Bureau, H., Ozawa, H., Garbarino, G., 2010. Melting of peridotite to 140 Gigapascals. Science 329 (5998), 1516–8.

Guillot, B., Sator, N., 2007. A computer simulation study of natural silicate melts. part II: High pressure properties. Geochimica et Cosmochimica Acta 71 (18), 4538–4556.

Hernlund, J. W., Jellinek, A. M., JUL 15 2010. Dynamics and structure of a stirred partially molten ultralow-velocity zone. Earth and Planetary Science Letters 296 (1-2), 1–8.

Hewitt, I. J., Fowler, A. C., 2008. Partial melting in an upwelling mantle column. Proceedings of Royal Society, A 464, 2467–2491.

Hier-Majumder, S., DEC 11 2008. Influence of contiguity on seismic velocities of partially molten aggregates. Journal of Geophysical Research-Solid Earth 113 (B12), B12205.

Hier-Majumder, S., 2011. Development of anisotropic mobility during two-phase flow. Geophysical Journal International 186, 59–68.

Hier-Majumder, S., Abbott, M. E., OCT 15 2010. Influence of dihedral angle on the seismic velocities in partially molten rocks. Earth and Planetary Science Letters 299 (1-2), 23–32.

Hier-Majumder, S., Courtier, A., 2011. Seismic signature of small melt fraction atop the transition zone. Earth and Planetary Science Letters 308 (3-4), 334–342.

Hier-Majumder, S., Revenaugh, J., NOV 1 2010. Relationship between the viscosity and topography of the ultralow-velocity zone near the core-mantle boundary. Earth and Planetary Science Letters 299 (3-4), 382–386.

Hier-Majumder, S., Ricard, Y., Bercovici, D., AUG 30 2006. Role of grain boundaries in magma migration and storage. Earth and Planetary Science Letters 248 (3-4), 735–749.

Holtzman, B. K., Zimmerman, M. E., Groebner, N., Ginsberg, S., Kohlstedt, D. L., 2003. Stress-driven melt segregation in partially molten rocks. Geochemistry, Geophysics, Geosystems 4 (5).

Jellinek, A., Manga, M., 2004. Links between long-lived hotspots, mantle plumes D$''$, and plate tectonics. Reviews of Geophysics 42 (RG3002).

King, D. S. H., Hier-Majumder, S., Kohlstedt, D. L., 2011. An experimental study of the effects of surface tension in homogenizing perturbations in melt fraction. Earth and Planetary Science Letters 307 (3-4), 735–749.

Mao, W. L., Mao, H.-K., Sturhahn, W., Zhao, J., Prakapenka, V. B., Meng, Y., Shu, J., Fei, Y., Hemley, R. J., 2006. Iron-rich post perovskite and the origin of the ultra low velocity zone. Science 312, 564–565.

McKenzie, D., 1984. The generation and compaction of partially molten rock. Journal of Petrology 25, 713–765.

McNamara, A. K., Garnero, E. J., Rost, S., OCT 15 2010. Tracking deep mantle reservoirs with ultra-low velocity zones. Earth and Planetary Science Letters 299 (1-2), 1–9.

Ohtani, E., Maeda, M., 2001. Density of basaltic melt at high pressure and stability of the melt at the base of the lower mantle. Earth and Planetary Science Letters 193, 69–75.

Olson, P., Christensen, U., 1986. Solitary wave propagation in a fluid conduit within a viscous matrix. Journal of Geophysical Research, B, Solid earth and Planets 91, 6367–6374.

Park, H. H., Yoon, D. K., 1985. Effect of dihedral angle on the morphology of grains in a matrix phase. Metallurgical Transactions, A 16 A, 923–928.

Rabinowicz, M., Ricard, Y., Grégoire, M., 2002. Compaction in a mantle with a very small melt concentration: Implications for the generation of carbonatitic and carbonate-bearing high alkaline mafic melt impregnations. Earth and Planetary Science Letters 203, 205–220.

Ricard, Y., Bercovici, D., Schubert, G., 2001. A two-phase model for compaction and damage; 2, Applications to compaction, deformation, and the role of interfacial surface tension. Journal of Geophysical Research, B, Solid Earth and Planets 106 (5), 8907–8924.

Richter, F., McKenzie, D., 1984. Dynamical models for melt segregation from a deformable matrix. J. Geol. 92, 729–740.

Rost, S., Garnero, E. J., Thorne, M. S., Hutko, A. R., Apr. 2010. On the absence of an ultralow-velocity zone in the North Pacific. Journal of Geophysical Research 115 (B4), 1–12.
URL http://www.agu.org/pubs/crossref/2010/2009JB006420.shtml

Rost, S., Garnero, E. J., Williams, Q., 2006. Fine-scale ultralow-velocity zone structure from high frequency seismic array data. Journal of Geophysical Research, B 111 (B09310).

Rudge, J. F., Bercovici, D., Spiegelman, M., 2011. Disequilibrium melting of a two phase multicomponent mantle. Geophysical Journal International, 699–718.

Schubert, G., Olson, P., Anderson, C., Goldman, P., 1989. Solitary Waves in Mantle Plumes. Journal of Geophysical Research Solid Earth 94 (B7), 9523–9532.

Scott, T., Kohlstedt, D., 2006. The effect of large melt fraction on the deformation behavior of peridotite. Earth and Planetary Science Letters 246 (3-4), 177–187.

Spiegelman, M., 1993. Flow in deformable porous media, part 1, Simple analysis. Journal of Fluid Mechanics 247, 17–38.

Sramek, Ricard, Y., Bercovici, D., 2006. Simultaneous melting and compaction in deformable two-phase media. Geophysical Journal International 168, 964–982.

Stixrude, L., Karki, B., 2005. Structure and freezing of $MgSiO_3$ liquid in Earth's lower mantle. Science 310,, 297–299.

Takei, Y., 1998. Constitutive mechanical relations of solid-liquid composites in terms of grain boundary contiguity. Journal of Geophysical Research 103, 18,183–18,203.

Takei, Y., 2002. Effect of pore geometry on v_p/v_s: From equilibriium geometry to crack. Journal of Geophysical Research 107, 2043.

Takei, Y., Hier-Majumder, S., OCT 30 2009. A generalized formulation of interfacial tension driven fluid migration with dissolution/precipitation. Earth and Planetary Science Letters 288 (1-2), 138–148.

von Bargen, N., Waff, H., 1986. Permeabilities, interfacial areas and curvatures of partially molten systems: results of numerical computations of equilibrium microstructures. Journal of Geophysical Research 91, 9261–9276.

Wicks, J. K., Jackson, J. M., Sturhahn, W., Aug. 2010. Very low sound velocities in iron-rich (Mg,Fe)O: Implications for the core-mantle boundary region. Geophysical Research Letters 37 (15), 1–5.
URL http://www.agu.org/pubs/crossref/2010/2010GL043689.shtml

Williams, Q., Garnero, E., 1996. Seismic evidence for partial melt at the base of Earth's mantle. Science 273, 1528–1530.

Wimert, J. T., Hier-Majumder, S., 2012. A three-dimensional microgeodynamic model of melt geometry in the earth's deep interior. Journal of Geophysical Research-Solid Earth 117 (B04), B04203.